Made available through Montana State University's ScholarWorks

Environmental controls on the kinetics of iron‐sulfur cluster nucleation and nanoparticle formation

Manjinder Kour; Heather M. Callaway; Eric S. Boyd

Accessibility Disclaimer:

For a more accessible version of this document, please submit an accessibility request form through the Montana State University Library website.

J Nanopart Res (2025) 27:256
https://doi.org/10.1007/s11051-025-06445-5

RESEARCH

Environmental controls on the kinetics of iron-sulfur cluster nucleation and nanoparticle formation

Manjinder Kour · Heather M. Callaway · Eric S. Boyd

Received: 9 August 2025 / Accepted: 2 September 2025 / Published online: 23 September 2025
© The Author(s) 2025

Abstract Anoxic, sulfidic conditions have been prevalent since the early Proterozoic and favor aqueous iron-sulfur (FeS_{aq}) clusters as a major fraction of the soluble, reduced iron and sulfur pool. FeS_{aq} cluster formation and nucleation is driven by the high affinity between ferrous iron (Fe(II)) and sulfide (HS^-), ultimately yielding particles that precipitate as iron sulfide minerals. FeS_{aq} clusters were recently shown to be bioavailable sources of iron and sulfur for a variety of anaerobes, yet little is known of the factors that influence the kinetics of their formation and nucleation. Here we apply computational and spectroscopic approaches to investigate the dynamics of FeS_{aq} nucleation, cluster growth, precipitation, and redissolution as a function of Fe(II)/HS^- concentration, temperature, and pH. Experiments were conducted under excess HS^- to mimic euxinic conditions common to contemporary anaerobic aquatic ecosystems and those of the Proterozoic. Density functional theory calculations reveal the key role of water oxygen-iron interactions in stabilizing small FeS_{aq} clusters and promoting solubility. Dynamic light scattering revealed a concentration-dependent increase in the kinetics of FeS_{aq} nucleation and cluster aggregation. Increasing temperature promoted FeS_{aq} cluster nucleation and aggregation while also enhancing dissolution. Alkaline pH also promoted FeS_{aq} nucleation and cluster aggregation. At 25 °C, pH 7.0, and at reactant concentrations of 30 µM, FeS_{aq} clusters < 10 nm in diameter remained in solution for > 2 h. These results underscore the importance of temperature, pH, and reactant concentration in the kinetics of FeS_{aq} nucleation and cluster growth that, in turn, influence their bioavailability in anaerobic ecosystems.

Keywords Mackinawite · Iron sulfide · Nanoparticle · Density functional theory · Dynamic light scattering · Nanoparticle · Cluster growth · Aquatic ecosystems

Introduction

The chemistry of soluble transition metals in anoxic systems is largely controlled by reactions involving reduced sulfur compounds such as sulfide (HS^-). Paramount among these metals is the ferrous iron (Fe(II)) ion that readily reacts with HS^- to form soluble (aqueous) multinuclear clusters (FeS_{aq}) (Eq. 1) [1, 2]. FeS_{aq} is widespread in a variety of anoxic compartments in marine and estuarine environments [3–6], deep ocean hydrothermal vent fluids

Supplementary Information The online version contains supplementary material available at https://doi.org/10.1007/s11051-025-06445-5.

M. Kour · H. M. Callaway · E. S. Boyd (✉)
Department of Microbiology and Cell Biology, Montana State University, Bozeman, MT, USA
e-mail: eric.boyd@montana.edu

H. M. Callaway
Department of Chemistry and Biochemistry, Montana State University, Bozeman, MT, USA

[5], freshwater lakes [7], terrestrial sediment porewaters [8], as well as riparian[9] and vadose zone fluids [10], among others. FeS_{aq}, as well as other transition metal clusters/complexes, have been suggested to be the primary form of reduced, soluble metals in many anaerobic ecosystems [11, 12], and likely have had a key role in metal transport since early in Earth history. Prior to > 2.4 Gya, ocean basins were ferruginous, with Fe(II) concentrations exceeding those of HS^- [13, 14]. This would have created conditions of HS^- limitation due to the thermodynamic drive to form FeS_{aq} and ultimately more stable and increasingly less soluble phases such as mackinawite ($FeS_{mack)}$ and pyrite (FeS_2). In contrast, during the Proterozoic 2.4 to 0.6 Gya, ferruginous conditions began to give way to euxinic conditions where HS^- concentrations exceeded those of Fe(II) (e.g., in ref. [15–18]). Such sulfidic conditions can lead to Fe(II) limitation due to the thermodynamic drive to form FeS_{aq}.

Consistent with their prevalence and importance in anoxic environments over geological history, in particular during the Proterozoic, FeS_{aq} likely also serve as building blocks in the formation of iron-sulfur minerals [19, 20]. FeS_{aq} clusters are predicted to be relatively stable, small (< 1000 nm), and soluble when concentrations of reactants are low (< 2 µM) [21]. However, at higher reactant concentrations (e.g., > 10 µM), FeS_{aq} nucleation is increasingly favored and can result in the condensation of FeS_{aq} to form FeS_{mack} and eventually FeS_2 via Eqs. 2 to 4 [22–25].

$$Fe(II)_{(aq)} + HS^-_{(aq)} \rightarrow FeS_{(aq)} + H^+ \quad (1)$$

$$FeS_{(aq)} \rightarrow nFeS_{(aq)} \quad (2)$$

$$nFeS_{(aq)} \rightarrow FeS_{(mack,\,s)} \quad (3)$$

$$FeS_{(mack,\,s)} + HS^-_{(aq)} \rightarrow FeS_{2(s)} + 0.5H_{2(g)} \quad (4)$$

Previous studies have employed Density Functional Theory (DFT) and small-angle X-ray scattering (SAXS) and potentiometric titrations with surface complexation modeling to probe the structure, surface, and the early stages of FeS. [26–28] These studies established key properties of FeS_{mack} including its metallic, non-magnetic bulk nature and its S-terminated {001} surface as the dominant low-energy surface (0.07 J m^{-2}) [26]. In situ SAXS further revealed that FeS_{mack} forms via a nonclassical pathway, in which primary FeS_{nano} particles assemble into mass-fractal aggregates that undergo oriented attachment and layer into the metastable phase [29]. Dispersion-corrected DFT also showed that incorporation of transition metals is favored through Fe-site substitution, which modulates lattice parameters and interlayer spacing [27]. These advances in bulk and surface FeS set the stage for probing hydrated FeS_{aq} clusters, the soluble precursors to solid phases, whose behavior under environmental conditions had not yet been addressed. Understanding the kinetics of FeS_{aq} formation and nucleation and transition towards metastable phases such as FeS_{mack} and FeS_2 (Eqs. 1–4) takes on additional importance considering that a variety of anaerobes, including methanogens [30–35], have been shown to use FeS_{aq} as a source of Fe and S. Similarly, fermenters, fumarate-respirers, and sulfate-reducing bacteria have been demonstrated to use FeS_{aq} clusters as sources of Fe and S for biosynthesis of vitamins, amino acids, and cofactors [36]. Members of these anaerobic guilds inhabit a range of anoxic environments, both today and in the geologic past, including marine and freshwater sediments, hydrothermal vents, subsurface ecosystems where Fe(II) and HS^- co-exist and where FeS_{aq} are likely to be the predominant form of bioavailable Fe and/or S [21]. The use of FeS_{aq} as sources of Fe and S in a variety of anaerobes is perhaps not surprising given their apparent prevalence in anoxic environments and their structural and chemical similarity to iron-sulfur cofactors in metalloenzymes [25, 36] that function in catalysis, electron transfer, and chemical sensing in all forms of life [37, 38].

At circumneutral pH, FeS_{aq} are thought to be neutrally charged which may enable their diffusion across the membrane in a manner similar to diatomic gases such as hydrogen, oxygen, and nitrogen [31, 35]. However, for this to be effective, FeS_{aq} would need to be of small diameter, especially considering the generally small (several µm diameter) size of microbial cells. Despite the importance of FeS_{aq} as a predominant soluble Fe(II) and/or reduced S phase in anaerobic ecosystems, little is known of the kinetics of FeS_{aq} nucleation, growth, aggregation, and redissolution. This is a critical knowledge gap with implications for the distribution, function, and activity of anaerobes in

anaerobic ecosystems. Here, the kinetics of FeS_{aq} formation are investigated under controlled conditions, with a focus on how environmental variables such as Fe(II)/HS^- concentration, reaction temperature, and fluid pH influence cluster and particle formation and redissolution. Results are discussed as they relate to metal transport and acquisition in anaerobic microbial ecosystems.

Materials and methods

Computational chemistry

Geometry optimizations were performed using DFT with the WB97xD functional [39] and def2-TZVP [40] basis sets. The initial structure of FeS_{mack} was sourced from the Inorganic Crystal Structure Database (ICSD) to ensure accurate representation of the starting material [41]. All calculations were executed using the Gaussian 16 software suite [42], with standard convergence criteria applied for the geometry optimizations. Broken-symmetry calculations were employed to model the antiferromagnetically coupled (AFC) system [43–45]. The solvent density-based (SMD) polarizable continuum model was used for implicit solvation of the clusters [46]. The optimized geometries were validated as local minima through the confirmation of no imaginary frequencies in subsequent vibrational analyses. Chemcraft software was used to analyze and visualize the optimized structures, facilitating detailed examination of the molecular geometries and interactions (https://chemcraftprog.com/).

Reaction buffer selection

All glassware used in experiments was soaked in trace metal-grade nitric acid for 24 h and then rinsed a minimum of three times with Milli-Q (MQ) water (18.2 MΩ-cm). All chemicals used in experiments were ACS-grade or higher. Several buffers (pH 7.0) were examined for use in experiments aimed at measuring FeS_{aq} cluster formation: sodium bicarbonate, sodium phosphate, and Tris-Base (tris(hydroxymethyl)aminomethane). Each buffer was prepared by dissolving an amount to generate a final concentration of 1 mM or 100 µM in an initial ~ 95 mL of anoxic MQ water, as specified. Anoxic MQ water was prepared by sparging the solution with N_2 passed over heated (210 °C) and H_2-reduced copper shavings using a needle cannula. All manipulations of anoxic solutions were conducted inside an anaerobic chamber (Coy Labs, Grass Lake, MI). The pH of buffer solutions was adjusted to 7.0 by adding anoxic 0.1 N HCl. Once pH 7.0 was attained, the volume was adjusted to 100 mL with anoxic MQ water. Ferrous chloride tetrahydrate ($FeCl_2{\cdot}4H_2O$) was added to a final concentration of 80 µM, and the pH was again measured to evaluate the effectiveness of each buffer. Dynamic light scattering (described below) was used to evaluate particle formation once Fe(II) was added to each buffer. Solutions were also filtered (20 nm) followed by determination of Fe(II) concentration in filtrate via the ferrozine assay to further evaluate the potential for particle formation and buffer component complexation with Fe(II). All solutions were filtered using Whatman Anotop 10 syringe filters [0.02 µm pore size; aluminum oxide membrane; Cytiva, Marlborough, MA, USA].

Dynamic light scattering (DLS) of FeS_{aq} clusters

Separate solutions of Fe(II) and HS^- were prepared using $FeCl_2{\cdot}4H_2O$ and sodium sulfide nonahydrate ($Na_2S{\cdot}9H_2O$), respectively. Solutes were dissolved in serum bottles containing 100 mL of anoxic MQ H_2O in the Coy chamber, as described above. $FeCl_2$ and Na_2S solutions were individually filtered through 20 nm filters to remove particulate matter prior to their use in DLS measurements. DLS measurements of FeS_{aq} formation and nucleation were initiated by mixing 1 mL $FeCl_2$ (to generate specified final concentration) prepared in 100 µM Tris-Base buffer (pH 7.0) with 1 mL of Na_2S (to generate specified final concentration) prepared in 100 µM Tris-Base buffer (pH 7.0). Immediately following the mixing of the two solutions, a 4 µL aliquot was transferred into a microcuvette (Wyatt Technologies, WNDMC) equipped with gas-tight septum cuvette. DLS measurements were conducted using a Nanostar model 4646 DLS (Wyatt Technology, Goletta, Georgia) at a temperature of 25 °C, unless otherwise specified. Particle size distribution data obtained from DLS measurements were processed with Dynamics software provided by the instrument manufacturer.

DLS is based on the measurement of laser light that has been scattered by particles in solution due

to Brownian motion [47]. This method precisely captures the time autocorrelation function (ACF) of the intensity of the scattered light, a mathematical construct that represents the collective motion of particle ensembles via their decay rates. These rates in turn provide information about an apparent mean diffusion constant, which is essential in determining particle diameter using the Stokes-Einstein equation [48]. This equation links the diffusion coefficient of particles (D_t) to their hydrodynamic radius and can be expressed as:

$$D_\tau = \frac{k_B T}{6\pi\eta R_h}$$

where k_B signifies the Boltzmann constant, T represents the absolute temperature of the sample, and η is the viscosity of the solution. This relationship underscores the inverse correlation between particle size and diffusion rate, establishing a direct path to measure particle size through light scattering experiments. The average hydrodynamic size calculated from DLS observations provides an intensity-weighted harmonic mean within the selected size range, allowing for the determination of particle size distributions within the solution.

Transmission electron microscopy (TEM)

Reactions were initiated by combining Fe(II) (30 µM) and HS^- (38 µM) in Tris-buffered (100 µM final, pH 7.0) MQ water and incubated at 25 °C. At 5 min, 15 min, and 60 min, 4 µL of the reaction mixture was deposited onto a glow-discharged 400-mesh carbon-coated copper grid (EMS CF-400CU). A Pelco easi-Glow instrument was used to glow discharge grids for 15 s. After loading the sample twice for 5 min, excess liquid was wicked away, and grids were air-dried in an anaerobic chamber prior to imaging. For the 15 min timepoint, the sample was reapplied to the grid every 5 min over a total reaction time of 15 min, and the excess liquid was wicked away. At 60 min, the sample was applied to the grid twice, and excess liquid was wicked away with Whatman filter paper (Whatman #1) after 5 min. All the grids were air-dried in an anaerobic chamber for 5 min prior to imaging. TEM analysis was performed using a Tecnai Spirit transmission electron microscope with a LaB_6 electron source operated at 120 keV and a Gatan UltraScan 1000 XP CCD camera. Data was collected at a magnification of 30,000×.

Results

FeS_{aq} cluster structure and size

DFT calculations were used to identify the optimum structure for FeS_{aq} clusters with specified stoichiometric units (*n*FeS). As the number of *n*FeS units was increased (e.g., 4FeS, 8FeS, 18FeS, 32FeS), the diameter of the clusters grew non-linearly (Fig. 1a) as captured by a second-order polynomial regression (Pearson R^2=0.98). Figure 1b shows a DFT-optimized $8FeS_{aq}$ cluster with water molecules interacting with the cluster via strong iron (Fe)-oxygen (O) bonds. The strong Fe–O bonds likely allow smaller FeS_{aq} clusters to remain in solution. Figure 1c illustrates the structural arrangement of FeS_{mack} sheets, formed through the nucleation of individual *n*FeS units. The depiction emphasizes the geometric arrangement of Fe and S atoms and illustrates how extended sheets of FeS_{mack} emerge from aggregated FeS_{aq} clusters. The Cartesian coordinates of DFT optimized FeS_{aq} clusters are provided in Supporting Information Table 1.

Explicit solvation of FeS_{aq}

To better understand how FeS_{aq} cluster nucleation relates to solubility, a solvation framework to examine how the adsorption energy (E_{ads}) of water varies with FeS_{aq} cluster size was generated (Fig. 2). Total energy calculations using DFT reveal that the smaller clusters readily stabilize in the presence of water. The smallest cluster, 2FeS, could only be successfully optimized when explicitly solvated, suggesting that hydration is critical for the stability of the smallest FeS_{aq} units. For $4FeS{\cdot}4H_2O$, the total E_{ads} was calculated to be − 102 kJ mol^{-1}. For larger clusters, E_{ads} energies became more negative, indicating stronger interactions, with a value of − 184 kJ mol^{-1} for $8FeS{\cdot}8H_2O$ in its layered configuration and − 280 kJ mol^{-1} for the same cluster in its sheet-like configuration. The layered $8FeS{\cdot}8H_2O$ has comparatively weaker hydration forces, but these forces are strong enough to keep the clusters explicitly solvated. The trend could continue until a point where transition

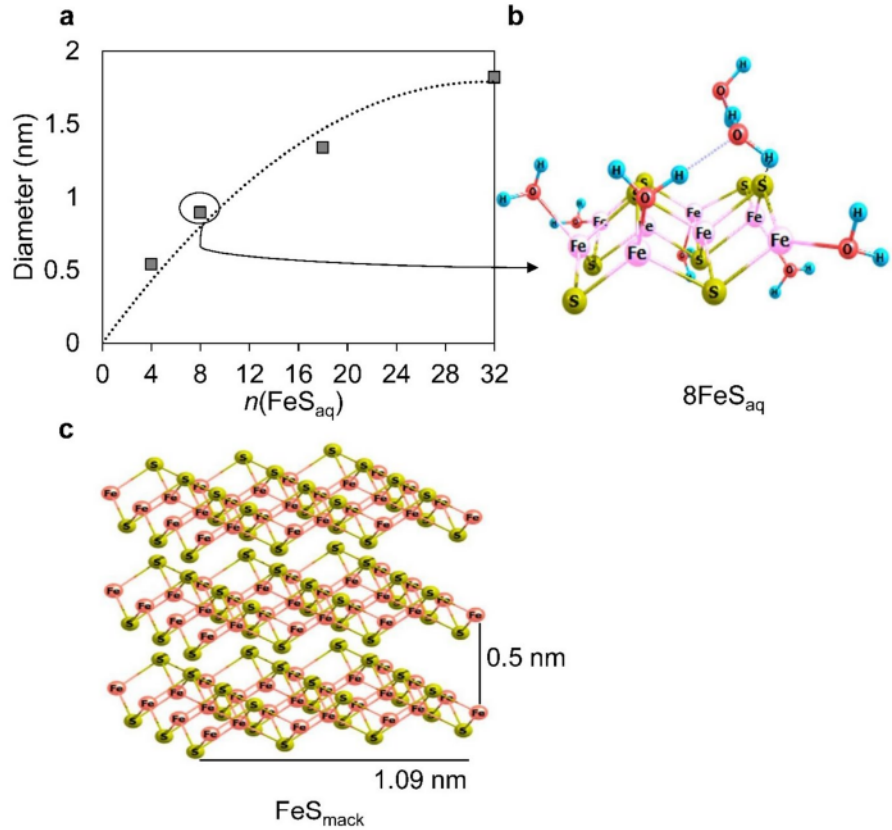


Fig. 1 The formation of mackinawite from the nucleation of aqueous iron-sulfur clusters (FeS_{aq}) generated via reaction of ferrous iron (Fe(II) with sulfide (HS^-). **a** The diameter (maximum length) of FeS_{aq} as a function of stoichiometric units (n) of FeS_{aq} (i.e., 4FeS, 8FeS, 18FeS, 32FeS) based on density-functional theory (DFT) calculations and bulk. Note that DFT calculations are for unit cells of nFeS$_{aq}$ (n=4, 8), and those cells form sheets as mackinawite mineral, which is not depicted. A second-order polynomial regression ($y=-0.0019x^2+0.1161x$) was used to relate diameter (in nm) to FeS_{aq} stoichiometric units (n), resulting in an R^2 of 0.98. **b** DFT-optimized structure of an 8FeS$_{aq}$ cluster. The water molecules are interacting with the cluster via iron (Fe)-oxygen (O) interactions. **c** Structural representation of mackinawite sheets (FeS_{mack}) based on crystallographic data (ICSD#15503) that depicts the arrangement of Fe and sulfur (S) atoms in the mackinawite crystal and that highlights the geometry and connectivity within each sheet. The model shows how individual FeS units polymerize and aggregate to form extended sheets during the mackinawite formation process. The nFeS units within these individual sheets are comparable to the stoichiometric units (nFeS) analyzed in Panel **a** in terms of connectivity and arrangement

toward bulk-like properties under appropriate conditions occurs.

To further examine how these interactions evolve with increasing FeS_{aq} cluster size, the E_{ads} energies were normalized per water molecule by dividing the total energy by the number of water molecules associated with the cluster. This normalization revealed that the smaller clusters exhibit strongly negative E_{ads} values (e.g., ≈ -26 kJ mol^{-1} per water molecule for 4FeS·4H_2O), indicating strong hydration forces. The sheet-like 8FeS·8H_2O exhibited a more favorable hydration energy ($E_{ads} \approx -35$ kJ mol^{-1} per water molecule) compared to the smaller cluster. In contrast, 8FeS·8H_2O in its layer configuration exhibits weaker hydration interactions ($E_{ads} \approx -23$ kJ mol^{-1} per water molecule). These results suggest that while larger clusters generally show a reduction in hydration strength per unit water molecule, structural configuration plays a key role, where sheet-like configuration may promote hydration and solubility more effectively than layered arrangements. Thermal enthalpies, which shift from -197 kJ mol^{-1} for the single layer 8FeS·8H_2O

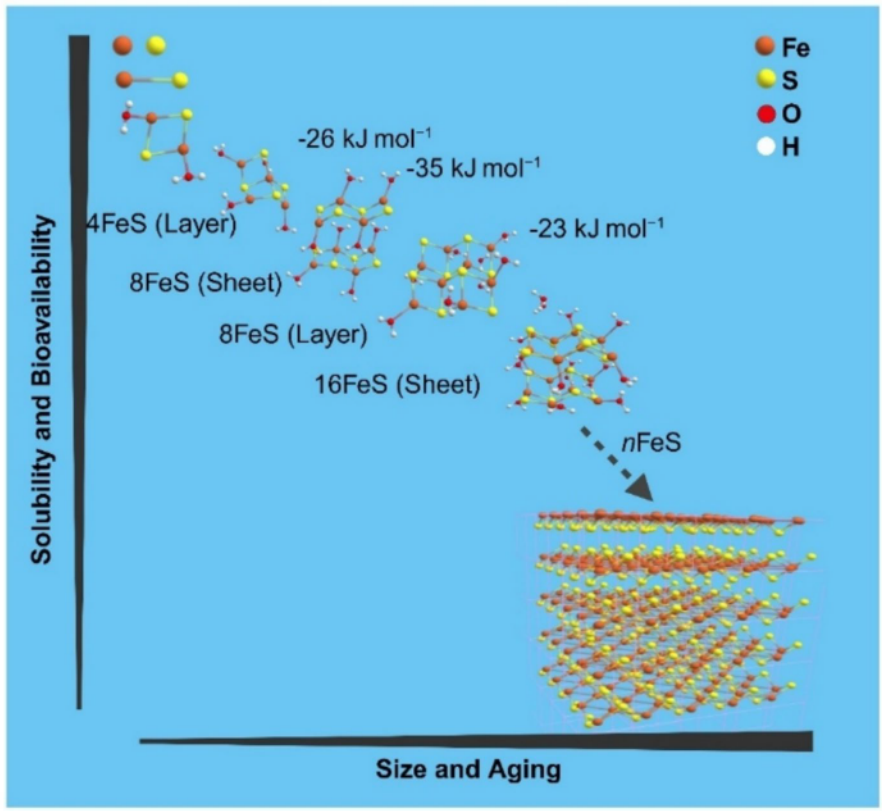


Fig. 2 Solubility of aqueous iron sulfur (FeS_{aq}) clusters, as inferred through adsorption energies (E_{ads}) per water molecule and as calculated using density functional theory (DFT). The blue background reflects the implicit solvation used to simulate the aqueous environment in calculations. The sheet/layer designation on the left refers to whether FeS_{aq} clusters structures consist of stacked sheets or a single layer. The E_{ads} values (shown on the right side) were derived as the difference between the total energy of the hydrated cluster and the sum of the energies of the isolated cluster and individual water molecules. Normalizing E_{ads} per water molecule enables direct comparison across clusters with varying degrees of hydration. The progressively less negative E_{ads} values indicate a weakening interaction as FeS_{aq} clusters increase in size, ultimately approaching a bulk *n*FeS structure resembling sheet-like mackinawite. Aging includes the slow progression from small clusters to larger bulk forms, illustrating the progression towards thermodynamically more stable and less soluble phases

to − 304 kJ mol^{-1} for the sheet-like configuration, further reinforce the trend. This finding indicates that sheet-like clusters are not only more strongly solvated but also thermodynamically more stable than their single-layer counterparts. These results demonstrate the relationship between FeS_{aq} cluster size, hydration dynamics, and solubility, and indicate that smaller clusters are soluble due to their strong interaction with water.

FeS_{aq} nucleation and growth kinetics

Effect of buffer on FeS_{aq} cluster/particle nucleation and growth

While DFT calculations show how *n*FeS unit nucleation impacts cluster/particle size, they reveal nothing about the kinetics of *n*FeS unit nucleation and particle growth. Further computational limitations associated

with DFT calculations constrain the size of clusters that could be subjected to solvation analyses, necessitating alternative experimental approaches to assess the transition from soluble, bioavailable forms to less soluble, aggregated states under varying conditions. To overcome these limitations and to begin to probe the kinetics of *n*FeS unit nucleation and particle growth, dynamic light scattering (DLS) was used.

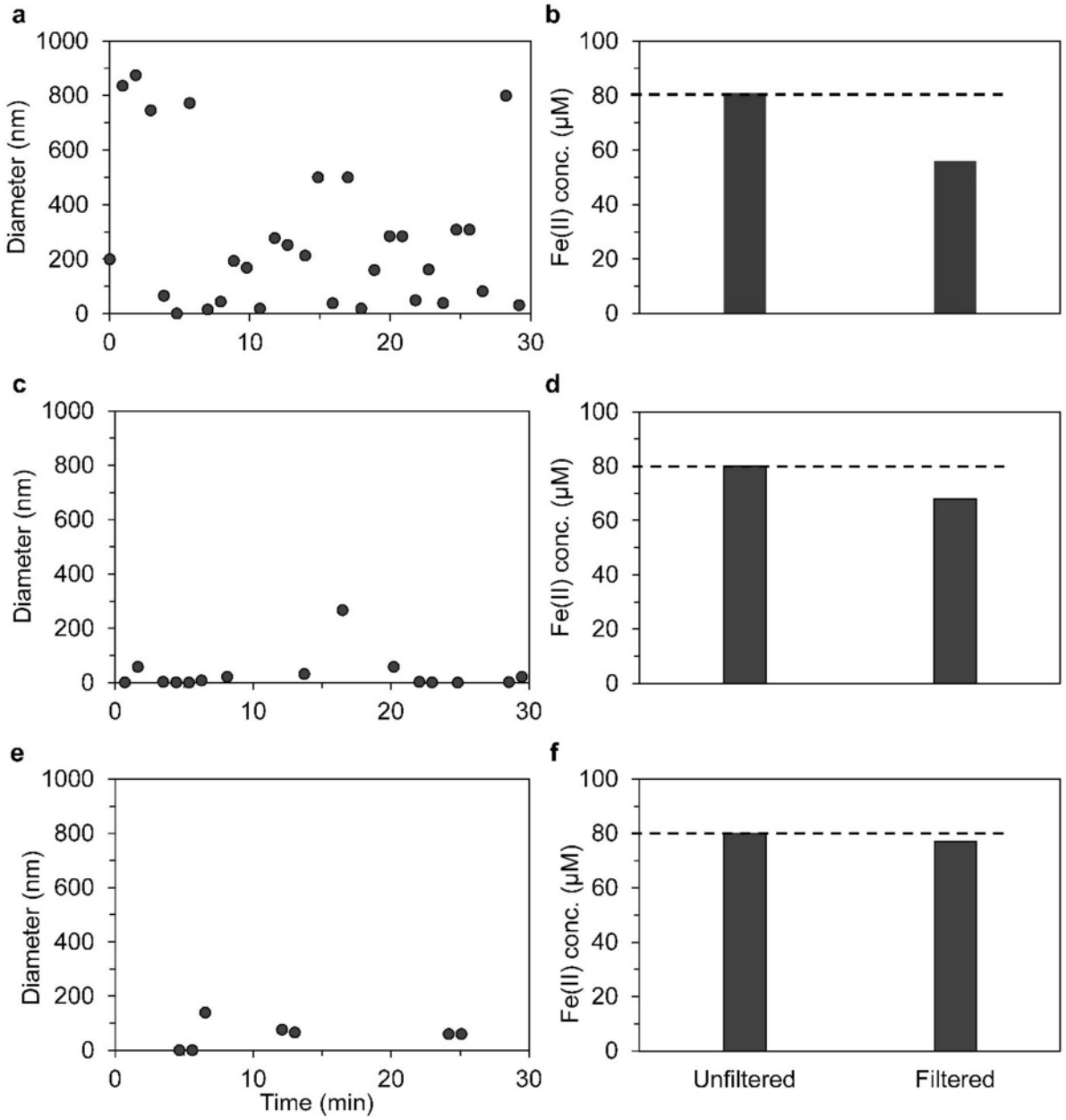


Fig. 3 The effect of buffer composition (1 mM final, pH 7.0) on complexation with ferrous iron (Fe(II)) and particle formation. Ferrous iron was added to a final concentration of 80 μM in sodium bicarbonate- (**a**), sodium phosphate- (**c**), or Tris-Base- (**e**) buffered Milli-Q water, and reactions were incubated at 25 °C. Particle growth was observed via dynamic light scattering. The effect of sodium bicarbonate (**b**), sodium phosphate (**d**), and Tris-Base buffers (**f**) on the concentration of Fe(II) in solution. Solutions were either filtered (< 20 nm) or unfiltered, and then Fe(II) was quantified via the ferrozine assay

However, prior to detailed characterization of *n*FeS nucleation and growth, it was first necessary to identify a suitable buffer that minimized interaction/complexation with Fe(II). Figure 3a, c, and e show the cluster/particle size distributions measured by DLS when 80 µM Fe(II) was added to MilliQ (MQ) water containing sodium bicarbonate, sodium phosphate, or Tris-Base buffer, respectively (each at a final concentration of 1 mM, pH 7.0). Figure 3b, d, and f show Fe(II) concentrations in filtered (< 20 nm) and non-filtered subsamples in each buffer type.

DLS indicated that the addition of Fe(II) to sodium bicarbonate buffer resulted in the formation of particles (Fig. 3a) and reduced the concentration of Fe(II) in 20 nm-filtered subsamples (Fig. 3b). This suggests Fe(II) and bicarbonate ion interact, leading to the formation of Fe(II) iron carbonate species, e.g., nanoparticulate siderite [49]. Addition of Fe(II) to sodium phosphate buffer also resulted in particle formation (Fig. 3c) and a reduction in free Fe(II) (Fig. 3d), although the extent of particle formation and complexation was less than that observed in the bicarbonate buffer. This indicates that both sodium bicarbonate and sodium phosphate promote Fe(II) complexation, reducing the availability of free Fe(II) for further reaction. In contrast, the addition of Fe(II) to Tris-Base buffer resulted in negligible particle formation (Fig. 3e) and nearly all of the Fe(II) remained in solution after filtration (Fig. 3f). Based on these results, Tris-Base was selected as the buffer (pH 7.0) for additional study of the kinetics of FeS_{aq} cluster formation, nucleation, and aggregation.

Modality of FeS_{aq} cluster/particles

It cannot be assumed that the reaction of two ionic species such as Fe(II) and HS^- will result in the formation of particles with uniform size. Therefore, prior to detailed experimentation, the size distribution and dispersity of FeS_{aq} clusters/particles formed from the reaction of Fe(II) and HS^- in Tris-Base buffer (1 mM, pH 7.0) were examined. Herein, *n*FeS units are operationally referred to as clusters during the nucleation and growth phases when they are smaller than 100 nm in diameter and when they are disordered and amorphous (discussed in more detail below). Further, *n*FeS are operationally referred to as particles in the growth aggregation phase when they exceed 100 nm in diameter. These particles exhibit reduced solubility and begin to show partial crystallinity (discussed in more detail below). When both FeS_{aq} clusters and particles are present, they are referred to as FeS_{aq} clusters/particles.

To probe particle distributions, an initial reaction was conducted at 25 °C with Fe(II) and HS^- concentrations of 80 µM and 100 µM, respectively, in Tris-base-buffered MQ water. DLS was used to measure cluster or particle size after 10 min (~0.16 h) of incubation. The results show distinct cluster/particle populations (Fig. 4a) thereby emphasizing the multimodality of the FeS_{aq} clusters, a feature that is characteristic of a heterogeneous nucleation and growth process [50–52]. The clusters/particles ranged in size from 10 to 1200 nm diameter, with the majority (indicated by % intensity or the proportion of light scattered) being in the range of 10 to 30 nm diameter. The data is presented as a histogram in Fig. 4b, further illustrating their multimodal nature. The percent polydispersity (%PD) value, which quantifies the variability in cluster/particle size, exceeds 15%. High %PD values, which were observed herein, suggest the presence of diverse cluster growth stages, from early nucleation events to more advanced aggregation events [50]. In simple words, if the large particle population is present in majority, it becomes difficult for DLS to discern the presence of smaller clusters at that time point as most of the light is scattered by the larger particles. To minimize overprinting of more abundant small clusters/particles by less abundant large particles, DLS data can be analyzed using the regularization method, as it provides a more detailed characterization of cluster populations in samples with significant heterogenicity [53]. Thus, further study of the kinetics of FeS_{aq} nucleation and aggregation were conducted and the data was analyzed using the regularization method.

Concentration-dependent effects on FeS_{aq} cluster/particle nucleation and growth

With buffer composition and the approach to data analysis optimized, experiments aimed at examining the effect of Fe(II) and HS^- concentration on the kinetics of FeS_{aq} nucleation and aggregation were performed. The concentration of buffer was decreased from 1 mM to 100 µM since pilot experiments indicated this lower concentration was sufficient to buffer additions of reactor components and that no

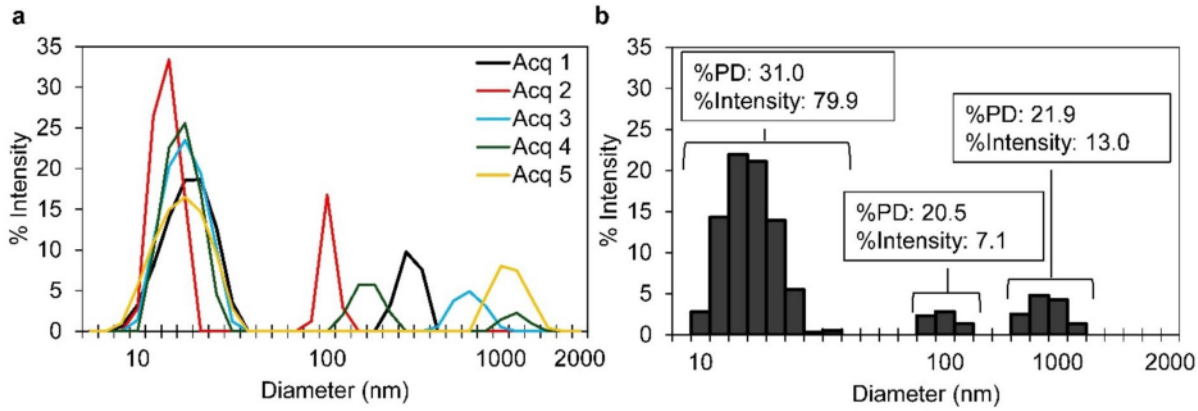


Fig. 4 Modality of aqueous iron-sulfur clusters (FeS_{aq}) and particles formed from the reaction of ferrous iron (Fe(II)) and sulfide (HS^-) as measured using dynamic light scattering. **a** Eighty µM Fe(II) and 100 µM HS^- were reacted for 10 min. (~0.16 h.) at 25 °C in Tris-Base-buffered (1 mM final, pH 7.0) Milli-Q water. Five sequential data acquisitions (Acq), each recorded over a period of 5 s, show the distribution of FeS_{aq} cluster/particle sizes (as percent (%) intensity). Percent intensity depicts the proportion of the total scattered light attributed to clusters/particles of a specific size range and demonstrates the polydispersity and multimodality of the clusters/particles. **b** Histogram illustrating the distribution of FeS_{aq} cluster/particle sizes further demonstrates their polydispersity. The % polydispersity (% PD) quantifies the variability in size distribution within a sample. A lower % PD indicates a more uniform size distribution, whereas % PD larger than 15% signifies a broader and more heterogeneous distribution of sizes. High % PD values reveal distinct cluster/particle populations and % Intensity values show the amount of light absorbed for each modality

complexation was observed via DLS (Supporting Information Fig. 1). The ratio of Fe(II) concentration to HS^- concentration in all experiments was kept constant at 4:5 and included the following: 30:38 µM, 40:50 µM, 50:63 µM, and 60:75 µM, all in Tris-Base-buffered (100 µM final, pH 7.0) MQ water incubated at 25 °C. Data are presented as the average hydrodynamic diameter of FeS_{aq} clusters/particles over time, and were segmented into "nucleation and growth" phase (cluster size < 100 nm) followed by a "growth and aggregation" phase (particle size > 100 nm), as operationally defined by inflection points in Fig. 5 and as discussed below.

Figures 5a to 5d show a concentration-dependent increase in the rate of FeS_{aq} cluster/particle growth and a concentration-dependent increase in the final size of FeS_{aq} cluster/particle. At concentrations of 30 µM Fe(II) and 38 µM HS^-, FeS_{aq} clusters reached diameters of approximately 10 nm after 30 min incubation and remained at that size for ~ 120 min (Fig. 5a). Only after 180 min incubation did the average FeS_{aq} cluster diameter reach 50 nm, with a maximum measured cluster size of 70 nm. As the concentration of Fe(II) and HS^- was increased to 40 and 50 µM, respectively (Fig. 5b), and 50 and 63 µM, respectively (Fig. 5c), the kinetics of the initial nucleation phase accelerated minimally. Clusters with an average diameter of 50 nm were observed after 130 and 140 min., respectively, with maximum cluster sizes reaching 130 nm and 150 nm, respectively. However, when the concentrations of Fe(II) and HS^- were increased to 60 and 75 µM, respectively (Fig. 5d), clusters with an average diameter of 50 nm were observed within 120 min, and particles reached a 210 nm average diameter by 180 min.

Regression analyses were applied to data reported in Fig. 5 to predict cluster/particle sizes at time points that could not be measured (< 6 min) and at lower reactant concentrations where determinations of cluster formation kinetics were not possible due to detection limits associated with the DLS instrument (Fig. 6). Experimental data measured from 6 to 30 min (presented in Fig. 5) were used to generate third-order polynomial regression models. These regressions provided estimates of FeS_{aq} cluster diameters in reactors at specified concentrations of Fe(II) and HS^-, allowing for extrapolation of cluster sizes at early time points that were not measurable (1 and 3 min) (Fig. 6a) and at low Fe(II)/HS^- concentrations (while maintaining a 4:5 ratio; Fig. 6b).

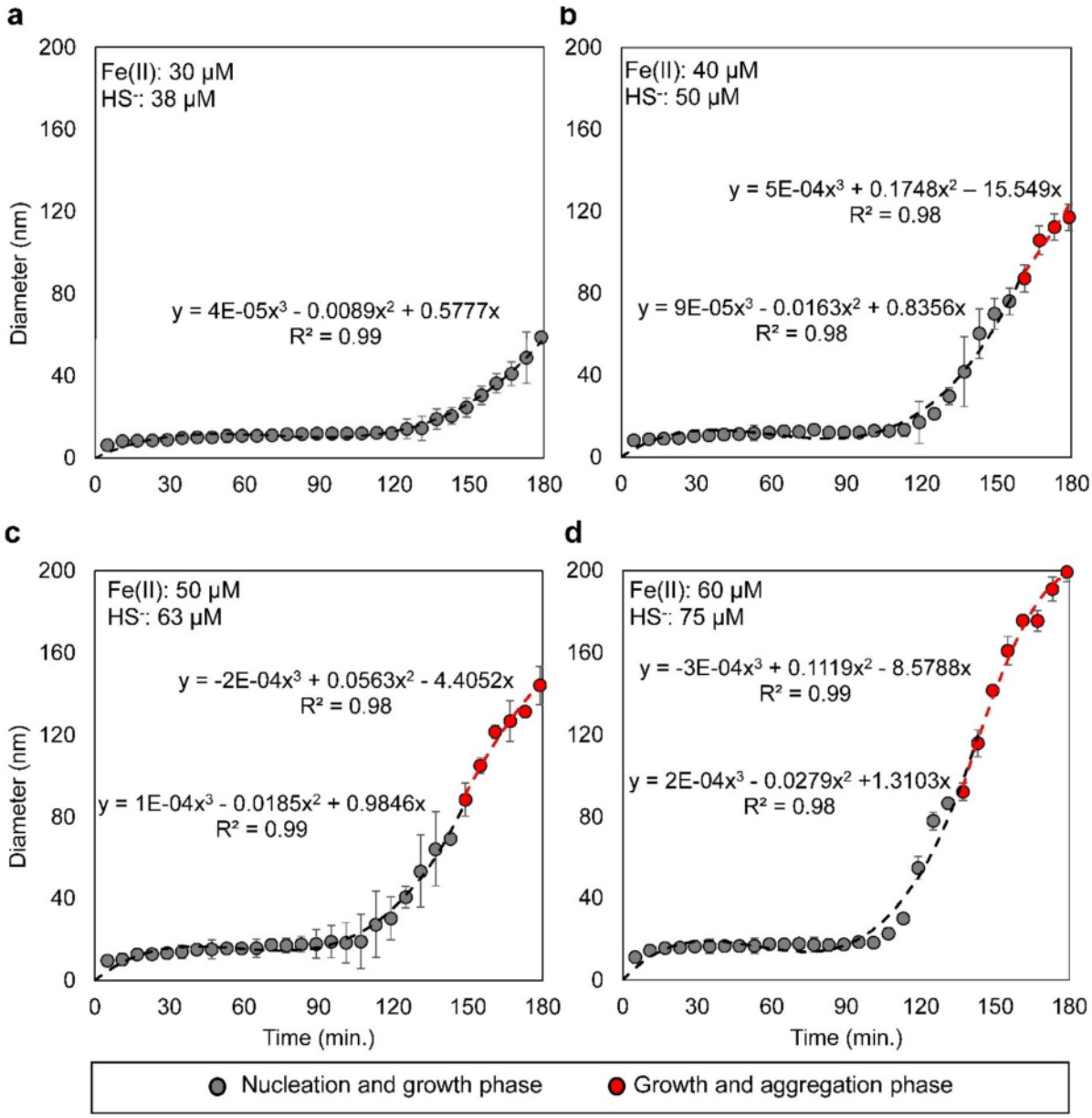
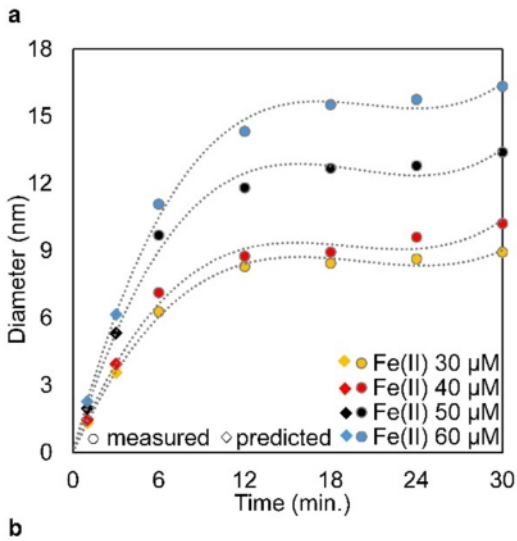
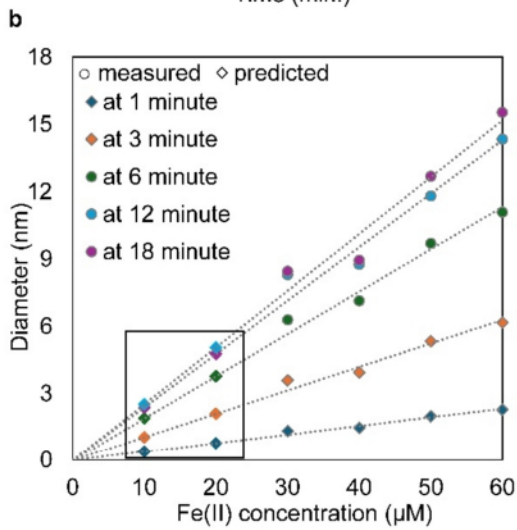


Fig. 5 Influence of reactant concentration on the kinetics of aqueous iron sulfur (FeS_{aq}) cluster/particle growth as measured using dynamic light scattering. Concentrations of ferrous iron (Fe(II)) in reactors were 30, 40, 50, and 60 µM, while concentrations of sulfide (HS^-) in reactors were 38, 50, 63, and 75 µM, respectively (4:5 ratio). Reactions were conducted in Tris-Base-buffered (100 µM final, pH 7.0) Milli-Q water at a temperature of 25 °C. Each panel (**a**–**d**) depicts the growth kinetics of FeS_{aq} at different Fe(II)/HS^- concentrations, showing the average cluster/particle diameter (nm) over time with error bars representing the experimental variability of three replicate reactions. Each dataset is segmented into two phases: nucleation and growth (gray circles) or growth and sheet aggregation (red circles). A third-order (cubic) polynomial regression was used to relate average cluster/particle size (diameter in nm) as a function of time for each of the four conditions with a forced Y axis intercept of 0



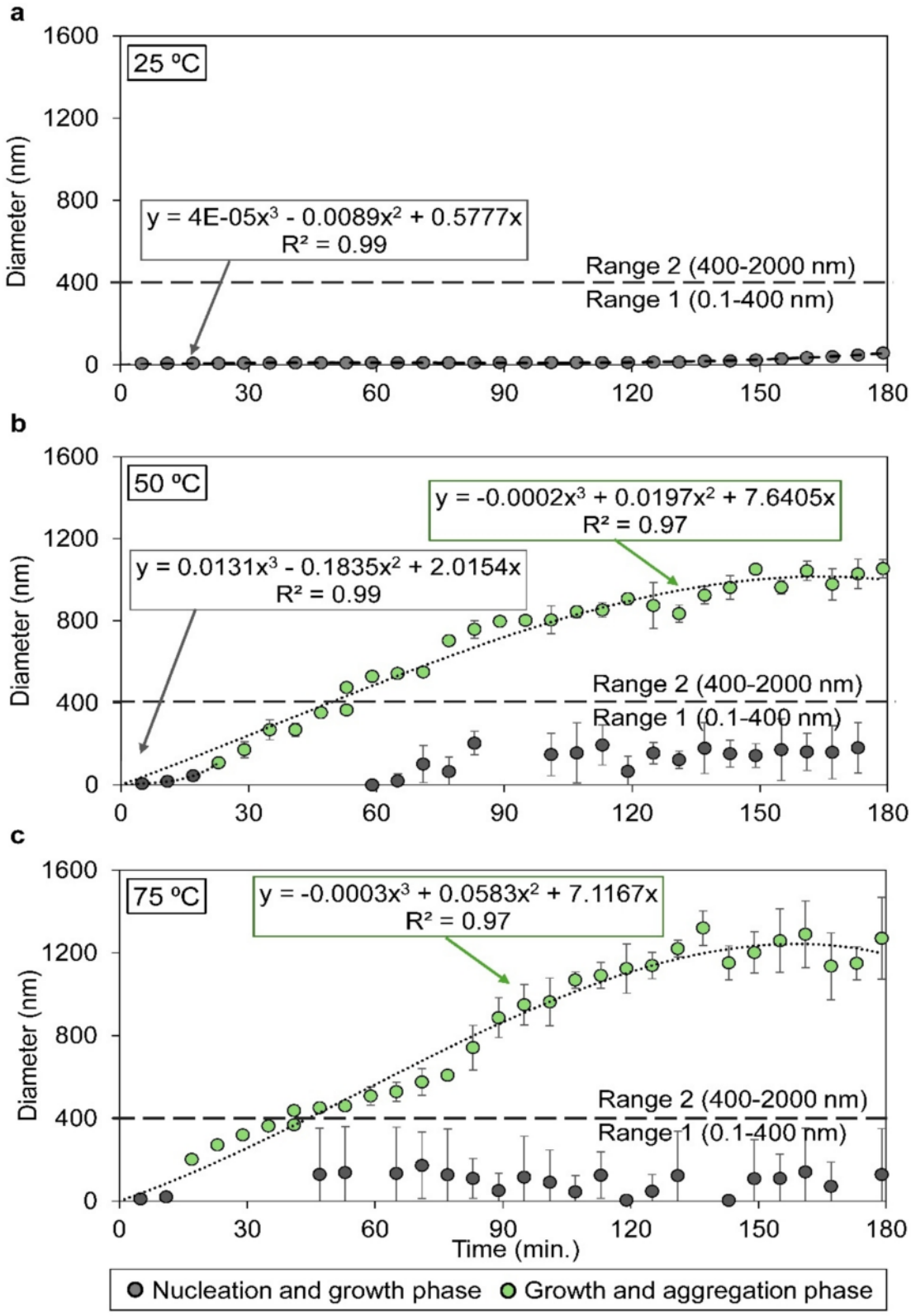
Plot a		
Conc. (Fe(II) + HS^-)	Regression eq. (y)	R^2
30 µM + 38 µM	$1.2E\text{-}03x^3\text{-}7.28E\text{-}02x^2\text{+}1.4025x$	0.98
40 µM + 50 µM	$1.5E\text{-}03x^3\text{-}8.39E\text{-}02x^2\text{+}1.5556x$	0.92
50µM + 63 µM	$1.8E\text{-}03x^3\text{-}1.098E\text{-}01x^2\text{+}2.0911x$	0.94
60 µM + 75 µM	$1.9E\text{-}03x^3\text{-}1.196E\text{-}01x^2\text{+}2.3955x$	0.98



Plot b		
Time	Regression eq. (y)	R^2
1 min	0.0389x	0.99
3 min	0.1049x	0.99
6 min	0.1888x	0.99
12 min	0.2383x	0.99
18 min	0.2531x	0.99

Fig. 6 Influence of reactant concentration on the kinetics of aqueous iron sulfur (FeS_{aq}) cluster/particle growth as measured using dynamic light scattering and as predicted using regression analyses. **a** FeS_{aq} cluster/particle growth (diameter in nm) over a 30-min period in reactors containing ferrous iron (Fe(II)) at concentrations of 30, 40, 50, and 60 µM and sulfide (HS^-) at concentrations of 38, 50, 63, and 75 µM, respectively, at a temperature of 25 °C (same data as in Fig. 4). Data points from 6 to 30 min (circles) were used to create a third-order (cubic) polynomial regression (forced Y axis intercept of 0) to predict cluster sizes at 1 and 3 min (diamonds). The regression equations fit to FeS_{aq} cluster/particle growth for each experimental condition are displayed with their respective R^2 values in the table to the right. **b** The relationship between Fe(II) concentration (at a 4:5 ratio with HS^-) and cluster/particle size at specific time points (1, 3, 6, 12, and 18 min). Linear regressions to relate cluster/particle size and concentration are shown alongside their R^2 values. Based on these linear equations, cluster/particle sizes were predicted at Fe(II) concentrations of 10 and 20 µM and HS^- concentrations of 13 and 25 µM, respectively, as highlighted within the boxed area. All regressions used a forced Y axis intercept of 0. Symbols are as follows: experimentally measured (circles), predicted (diamonds)

The calculations predicted formation of extremely small FeS_{aq} clusters (< 3 nm) regardless of Fe(II)/HS^- concentration. Further, calculations showed that higher Fe(II) concentrations yield somewhat faster nucleation kinetics, but the effect on cluster size early during the reaction is minimal. At Fe(II) concentrations of 30, 40, 50, and 60 µM and HS^- concentrations of 38, 50, 63, and 75 µM, initial cluster/particle size at 1 min was predicted to be approximately 1 to 2 nm, which would comprise ~ 16 FeS stoichiometric


a
25 ºC
y = 4E-05x³ - 0.0089x² + 0.5777x
R² = 0.99
Range 2 (400-2000 nm)
Range 1 (0.1-400 nm)
Diameter (nm)
b
50 ºC
y = -0.0002x³ + 0.0197x² + 7.6405x
R² = 0.97
y = 0.0131x³ - 0.1835x² + 2.0154x
R² = 0.99
Range 2 (400-2000 nm)
Range 1 (0.1-400 nm)
Diameter (nm)
c
75 ºC
y = -0.0003x³ + 0.0583x² + 7.1167x
R² = 0.97
Range 2 (400-2000 nm)
Range 1 (0.1-400 nm)
Diameter (nm)
Time (min.)
Nucleation and growth phase
Growth and aggregation phase

◂**Fig. 7** Growth kinetics of aqueous iron sulfur (FeS_{aq}) clusters/particles in reactors containing 30 µM ferrous iron (Fe(II)) and 38 µM sulfide (HS^-) as a function of incubation temperature as measured using dynamic light scattering. FeS_{aq} cluster/particle growth (diameter in nm) was measured over a 180-min period in reactors incubated at 25 °C (**a**), 50 °C (**b**), and 75 °C (**c**) in Tris-Base-buffered (100 µM final, pH 7.0) Milli-Q water. The data is divided into two phases: Nucleation and growth (gray circles) and growth and aggregation (green circles). Due to the complex growth trend, separate third-order (cubic) polynomial regressions were fitted to each phase, with their respective R^2 values provided. Due to the rapid rate of cluster FeS_{aq} nucleation at 75 °C, only the second phase of growth was modeled in **c**. The dashed line indicates that a regularized fit was chosen, with two size ranges selected (0.1–400 nm and 400–2000 nm)

units based on calculations depicted in Fig. 1. Predictions for lower Fe(II) concentrations, including 10 and 20 µM that could not be tested experimentally, indicate smaller cluster/particle sizes that remained small over extended (> 18 min) time periods. This is consistent with slower nucleation rates when reactants are diffuse (low concentration) in solution. These results demonstrate that smaller FeS_{aq} clusters are more likely to remain in solution and thus bioavailable for a longer time period.

To further monitor the formation of FeS_{aq} clusters, Ultraviolet–Visible (UV–Vis) spectroscopy was performed in Tris-buffered MQ water (100 µM, pH 7.0) containing Fe(II) at concentrations of 30, 40, 50, and 60 µM and HS^- at concentrations of 38, 50, 63, and 75 µM, maintaining an Fe(II):HS^- ratio of 4:5 (Supporting Information Fig. 2). UV–Vis absorbance scans were conducted every 3 min over the first 18 min of reaction. Two absorbance features were observed: a narrow peak near 285 nm and a broad peak in the visible region (400 to 700 nm). The 285 nm peak is attributed to the charge transfer band associated with formation of FeS_{aq} [54], whereas the broad absorbance at 400 to 700 nm is consistent with turbidity due to aggregation of particles and reflects their formation and growth [55, 56]. While absorbance remained relatively stable, with minor increases at 285 nm and no observable absorbance at 400 to 700 nm when 30 µM Fe(II) was reacted with 38 µM HS^-, higher concentrations of Fe(II) (40 µM, 50 µM and 60 µM), when added to HS^- (50 µM, 63 µM, 75 µM, respectively), showed increases in the absorbance of both features. This is consistent with DLS data indicating that higher concentrations of reactants lead to faster FeS_{aq} cluster nucleation and particle aggregation kinetics.

Temperature-dependent effects on FeS_{aq} cluster/particle nucleation and growth

Experiments were then conducted to examine the effect of temperature on FeS_{aq} cluster/particle nucleation and growth. Tris-buffered MQ water (100 µM, pH 7.0) containing Fe(II) and HS^- at concentrations of 30 µM and 38 µM, respectively, were incubated at 25 °C, 50 °C, and 75 °C, and cluster/particle size was monitored over a 180-min period using DLS (Fig. 7). The rate of FeS_{aq} cluster nucleation and growth was temperature-dependent. At 25 °C, FeS_{aq} clusters formed gradually, with the nucleation and growth phase extending over the 180 min incubation period. The average particle diameter never exceeded 100 nm during the incubation, similar to what was observed in Fig. 5a. At 50 °C, nucleation of FeS_{aq} occurred more rapidly and FeS_{aq} began to aggregate following only 15 min of incubation, with 400 nm average diameter particles observed within the first 60 min of incubation. Interestingly, while the average particle diameter continued to grow after 60 min, smaller (100 to 200 nm diameter) FeS_{aq} clusters/particles also became detectable. At 75 °C, FeS_{aq} cluster nucleation was nearly instantaneous, and aggregation began within the first 15 min of incubation, with the average particle size reaching > 400 nm diameter after only 40 min of incubation. Like reactors incubated at 50 °C, smaller FeS_{aq} clusters became detectable in reactors incubated at 75 °C. This suggests that temperature increases the rate of FeS_{aq} nucleation and aggregation into FeS_{mack} nanoparticles but also likely increases the rate of FeS_{mack} dissolution as nucleation/aggregation reactions approach equilibrium. This equilibrium may be more quickly reached at higher temperatures due to increased molecular motion.

To begin to evaluate the effect of temperature on FeS_{aq} cluster/particle dissolution, assays were conducted to initiate formation of FeS_{aq} clusters/particles by reacting 30 µM Fe(II) and 38 µM HS^-. Reactions were incubated at 25 °C, 50 °C, and 75 °C for varying time intervals (0, 30, and 60 min.), and the concentration of dissolved (operationally defined as < 20 nm) Fe(II) (or FeS_{aq} clusters smaller than 20 nm) was measured via the ferrozine assay following filtration (Fig. 8). The DLS partitioned the distribution into two ranges (0.1–400 nm and 400–2000 nm) when larger aggregates

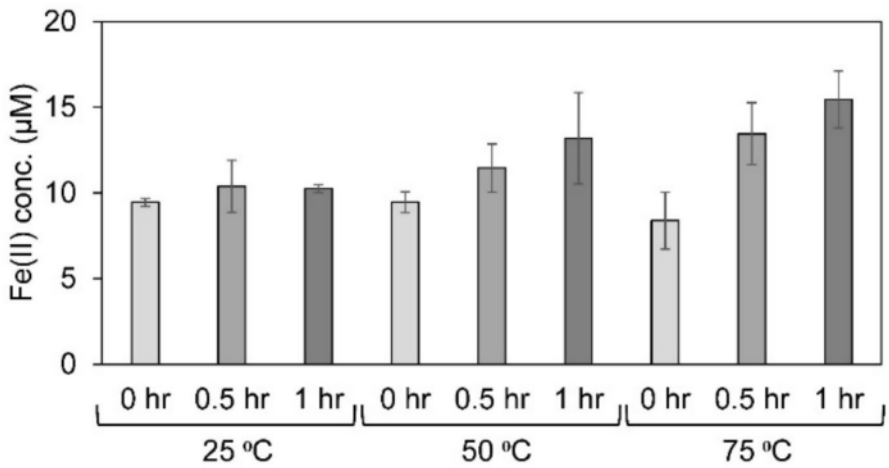


Fig. 8 Formation of aqueous iron sulfur (FeS_{aq}) clusters through reaction of 30 μM ferrous (Fe(II)) and 38 μM sulfide (HS^-) in Tris-Base-buffered (100 μM final, pH 7.0) Milli-Q water and their subsequent dissolution. Reactions were incubated at 25 °C, 50 °C, and 75 °C. Fe(II) concentration in filtrate (< 20 nm poresize) measured at 0, 30, and 60 min

were present; this separation reflects analytical constraints and does not alter our operational definitions of clusters (< 100 nm) and nanoparticles (> 100 nm).

The results show a temperature-dependent increase in the dissolution of FeS_{aq} clusters/particles. At 25 °C, Fe(II) concentrations remained relatively stable over the 60-min incubation, whereas at 50 °C, a gradual increase in Fe(II) concentration was observed. At 75 °C, Fe(II) concentrations increased sharply within the first 60 min of incubation. These observations indicate that temperature accelerates the dissolution of FeS_{aq} clusters and particles.

pH-dependent effects on FeS_{aq} cluster/particle nucleation and growth

Experiments were then conducted to determine the effect of pH on the kinetics of FeS_{aq} cluster/particle formation and growth. Reactors containing Tris-buffered (100 μM) MQ water at pH 7.0 and pH 8.0 were amended with Fe(II) and HS^- at concentrations of 30 μM and 38 μM, respectively, and were incubated at 25 °C. At pH 7.0, FeS_{aq} cluster nucleation, growth, and aggregation proceeded as observed in prior experiments, namely slow nucleation over the first 120 min of incubation with average particle sizes < 100 nm diameter even after 180 min of incubation (Fig. 9a). However, at pH 8.0, FeS_{aq} nucleation was completed within 60 min incubation and larger particles of ~ 265 nm diameter were observed by 120 min incubation (Fig. 9b).

FeS_{aq} cluster morphology and crystallinity

To examine qualitatively the morphology and crystallinity of FeS_{aq} clusters formed via reaction of Fe(II) and HS^-, transmission electron microscopy (TEM) was conducted at three time points following reaction initiation: 5 min, 15 min, and 60 min (Fig. 10). Samples were prepared in Tris-buffered MQ water (100 μM, pH 7.0) at Fe(II) and HS^- concentrations of 30 μM and 38 μM, respectively, and reactions were incubated at 25 °C. The TEM images reveal distinct differences in cluster size, morphology, and degree of crystallinity between different time points. At 5 min and 15 min, the FeS_{aq} clusters occurred predominantly as small, spherical, non-aggregates with an average size of less than 5 nm (Figs. 10a, b, and c). The FeS_{aq} clusters were generally amorphous, as indicated by the absence of diffraction fringes in TEM images. At 60 min, the FeS_{aq} clusters exhibited a multimodal size distribution, with a prevalence of small FeS_{aq} clusters and several large aggregates > 50 nm in diameter (Fig. 10c and Supporting Information Fig. 3). Diffraction fringes were observed around the edges of a few larger particles, suggesting partial crystallinity, while others retained their amorphous structure (Fig. 10d).

The transition from small, amorphous clusters to a multimodal distribution with partially crystalline aggregates reflects the progression from nucleation to growth and aggregation over time and is consistent with DLS and UV–Vis measurements presented above.

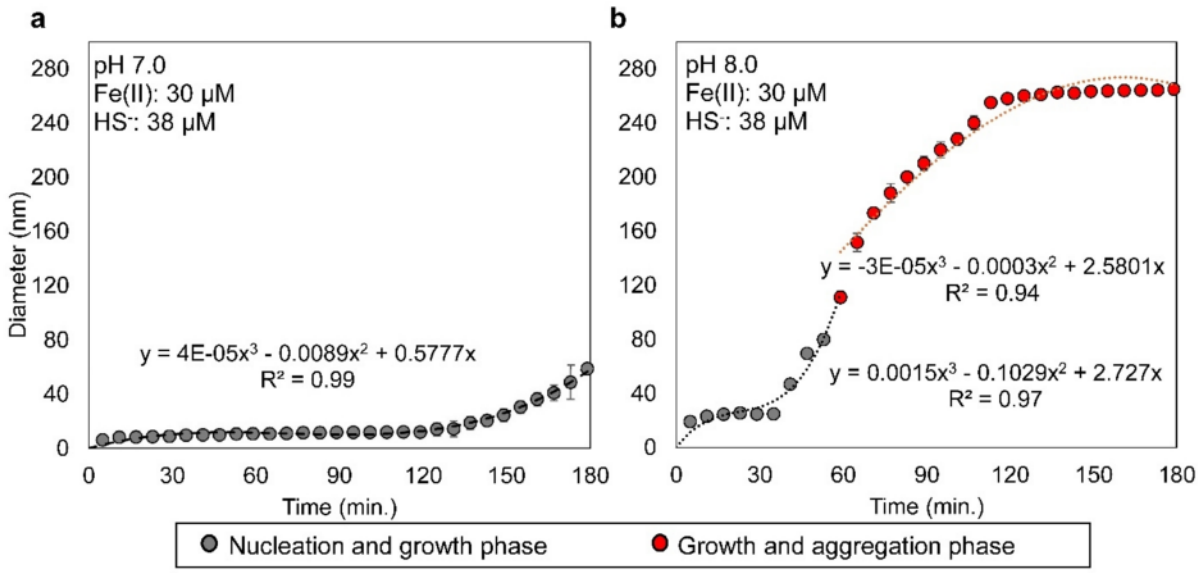


Fig. 9 Effect of pH on the growth kinetics of aqueous iron sulfur (FeS_{aq}) clusters/particles as measured using dynamic light scattering. Reactions contained 30 µM ferrous iron (Fe(II)) and 38 µM sulfide (HS^-) in Tris-Base-buffered (100 µM final) Milli-Q water at a temperature of 25 °C. Two pH conditions were tested: pH 7.0 (**a**) and pH 8.0 (**b**). The average FeS_{aq} cluster size (diameter in nm) is shown as a function of time, segmented into two phases: Nucleation and growth (gray circles) and growth and aggregation (red circles). A third-order (cubic) polynomial regression was applied to relate average cluster size as a function of time, with a forced Y axis intercept of 0

Discussion

DFT computations were used to provide insight into the size of *n*FeS during the initial stages of the FeS_{aq} cluster nucleation since these could not be measured due to limitations of DLS experimental measurement. DFT computations show a polynomial relationship between end-to-end cluster diameter and *n*FeS, with those comprising eight FeS units nearing one nm and those with 32 FeS units nearing 1.8 nm in diameter. During particle growth, *n*FeS will eventually organize into sheetlike structures; however, it is not clear at what crystallite size *n*FeS organizes as sheets. Our findings complement prior computational and experimental work on FeS, including DFT and surface-complexation studies that established fundamental bulk properties and reactive sites of FeS [26, 28, 29].

A combination of DLS, UV–Vis spectroscopy, and TEM imaging was used to experimentally evaluate the transition from smaller and soluble (bioavailable) forms of FeS_{aq} to larger and less soluble, aggregated states that presumably are less bioavailable. Observations presented in Fig. 5 show a positive relationship between Fe(II) and HS^- concentration and the kinetics of FeS_{aq} cluster nucleation and growth. Classical nucleation theory provides a framework for interpreting these results [57]. Higher concentrations of Fe(II) and HS^- ions accelerate nucleation rates, lowering the energy barrier for FeS_{aq} cluster formation. Consequently, as concentrations of reactants increase, the nucleation phase becomes shorter, and the transition to the growth and aggregation phase occurs more rapidly. This is evident from the size distributions, which show that lower reactant concentrations result in initially smaller FeS_{aq} clusters, with more time required for subsequent growth and aggregation. In line with theoretical expectations, the aggregation phase reflects an interplay between nucleation kinetics and aggregation or growth rates. The increased availability of nucleation sites at higher reactant concentrations leads to faster aggregation into larger particles. These findings reinforce the notion that concentration gradients play a critical role in determining FeS_{aq} cluster size, solubility, and thus availability for anaerobic microorganisms. They also likely influence transport, as smaller FeS_{aq} clusters would presumably be more mobile in anoxic systems. Beyond their role as precursors to mineral phases,

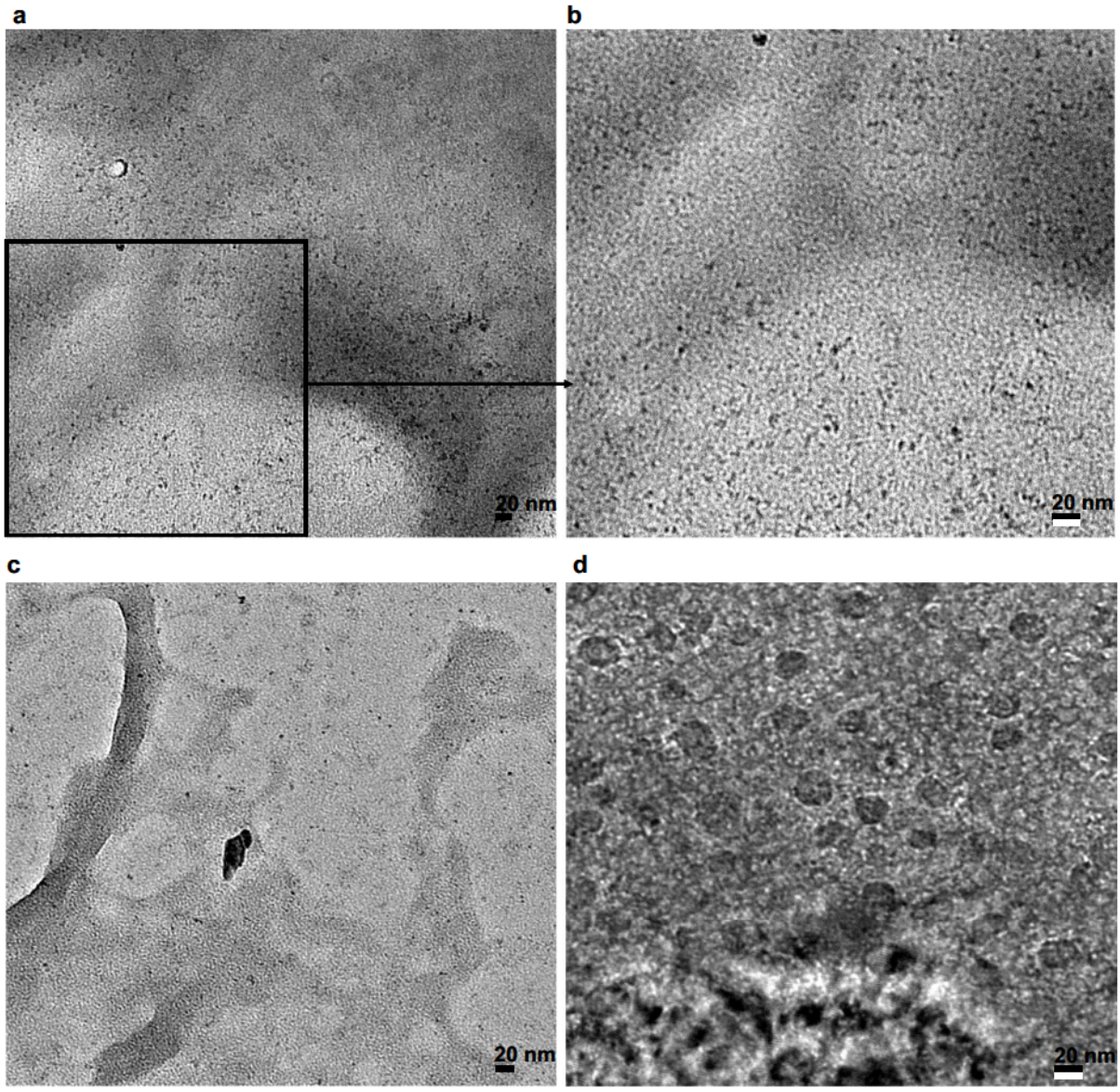


Fig. 10 Transmission Electron Microscopy (TEM) images of aqueous iron-sulfur (FeS_{aq}) clusters/particles. Reactors were initiated by addition of 30 µM ferrous iron (Fe(II)) and 38 µM sulfide (HS^-) in Tris-buffered (100 µM final, pH 7.0) Milli-Q water incubated at 25 °C. The subsamples were collected and imaged at **a** 5 min (scale bar 20 nm), **b** inset of **a** that is zoomed in to show detailed portion (scale bar 20 nm), **c** 15 min, and **d** 60 min (scale bar 20 nm). Imaging shows predominantly spherical and non-aggregated particles at 5 min and 15 min time points and a multimodal size distribution at 60 min. Some particles exhibit a diffraction glow line (fringes) around the edge, indicative of crystallinity, while others remain amorphous

the persistence of FeS_{aq} clusters and nanoparticles also has implications for colloid-mediated transport of Fe, S, and trace metals in natural waters [58–63]. Recent work has shown that FeS colloids generated during sulfidation reactions can remain suspended for extended periods, thereby enhancing the mobility of nutrients and contaminants in low salinity and low oxygen environments [58]. Our results provide complementary evidence that the stability of nm-scale FeS_{aq} clusters under environmentally relevant

conditions may serve as a critical first step in such transport processes.

The kinetics of FeS_{aq} cluster formation at the low Fe(II) and HS^- concentrations (e.g., < 20 µM of one or both reactants) that are relevant to many natural systems are challenging to test in the lab experimentally using DLS due to experimental logistics and instrument detection limitations. For example, FeS_{aq} clusters had nucleated and grown to diameters of ~ 6 nm within 6 min when 30 µM Fe(II) was reacted with 38 µM HS^-. Extrapolation of FeS_{aq} cluster formation to low (< 20 µM) Fe(II) concentrations showed that smaller FeS_{aq} clusters are predicted to form and nucleation is slow, resulting in clusters remaining small in size (< 3 nm) for extended periods (up to 20 min). Natural environments where reactant concentrations are in this range (< 20 µM) would likely enhance transport and use by anaerobic microorganisms.

Observations indicate that the equilibria between soluble FeS_{aq} clusters of varying sizes and nanoparticles are strongly influenced by temperature, with elevated temperatures shortening the nucleation phase and accelerating aggregation. Increased thermal energy lowers activation barriers and increases motion, resulting in more frequent interactions between ions and particles [64], thereby promoting faster cluster formation and subsequent aggregation. Studies have reported that higher temperatures enhance the iron-sulfide precipitation rates under observed conditions in various systems due to the promotion of reaction kinetics [65, 66]. At the same time, temperature impacts less stable "distorted tetragonal FeS" by decreasing its stability and increasing solubility [24, 28]. This contrasts with the behavior of crystalline and stable forms of minerals, such as cubane-type Fe_4S_4, which retain their structural integrity and resist thermal degradation at higher temperatures [67]. These findings underscore the dual role of temperature in FeS_{aq} cluster formation/aggregation and dissolution—higher temperature promotes dissolution of FeS_{aq} clusters/particles (Fig. 7) which leads to the generation of reactants that, in turn, promotes FeS_{aq} cluster formation and dissolution. This interplay may create transient windows of high FeS_{aq} cluster bioavailability during the nucleation and early growth phases, which anaerobes could take advantage of, in particular in high-temperature environments like marine hydrothermal vents (e.g., black smokers). It is worth noting that Fe(II), HS^-, and FeS_{aq} are commonly detected in marine hydrothermal environment emissions [68], potentially consistent with the prevalence of anaerobes, including methanogens and sulfate reducers in these environments (as reviewed in [69]), that have a high demand for iron-sulfur cofactors [70].

The faster nucleation and growth kinetics of FeS_{aq} clusters at pH 8.0 relative to pH 7.0 reflects the increased availability of HS^- ions due to the pKa of H_2S/HS^- being pH 7.0 at 25 °C [71]. HS^- is more reactive than H_2S[72] and thus promotes nucleation and aggregation (Fig. 9b). The deprotonated state of HS^- increases its electron density, allowing for faster and more efficient complexation with Fe(II). The energies of Frontier Molecular Orbitals (FMOs) are an important feature of the reactivity. It has been demonstrated in the past that the highest occupied molecular orbital (HOMO) of HS^- is less stable (−2.31 eV) and more accessible than that of H_2S (−10.47 eV) [73, 74]. As such, the HS^- species facilitates more facile electron donation during nucleation of FeS_{aq} clusters. These results are consistent with those of others that show more alkaline pH enhanced the rate of FeS_{aq} cluster nucleation and precipitation as amorphous iron sulfide or FeS_{mack}.[65].

TEM imaging of FeS_{aq} clusters provides direct evidence of the structural changes that accompany nucleation, growth, and aggregation. The images reveal diffraction fringes for some FeS_{aq} clusters/particles. In contrast, smaller clusters from the nucleation and growth phases lack such crystallinity, appearing as amorphous or poorly ordered structures. This distinction underscores a critical transition in the properties of FeS_{aq} clusters as they grow and aggregate. Previous studies have shown that less stable amorphous FeS nanoparticles and nanocrystalline FeS nanoparticles can coexist, with transitions between these phases driven by variations in redox potential, pH, and aging processes [50, 75]. While some particles larger than 100 nm exhibit crystalline domains, others in the same size range remain amorphous, which may be due to localized variability in conditions (e.g., reactant concentration) during the nucleation and growth phase. Importantly, TEM analysis also shows the persistence of particles smaller than 5 nm even during the later aggregation phase. These smaller clusters, which remain amorphous, suggest that dissolution and re-precipitation processes may sustain a reservoir of bioavailable FeS_{aq} clusters despite the formation of larger

particles and aggregates. The emergence of crystalline structures in larger particles aligns with theoretical predictions of thermodynamically driven aggregation processes, where the reduction in surface energy promotes the formation of ordered domains [76]. However, these crystalline particles are likely less bioavailable due to their reduced solubility and reactivity compared to smaller and amorphous clusters. This structural transformation, combined with the persistence of smaller clusters, highlights the dynamic equilibrium between growth, aggregation, and dissolution that likely governs Fe and S bioavailability in natural systems.

In conclusion, the results presented in this study offer new insight into the formation kinetics, solubility, and growth dynamics of FeS_{aq} clusters/particles under varied environmental conditions. The observed dynamics of nucleation, growth, and aggregation highlight how FeS_{aq} clusters transition from smaller, soluble and likely more bioavailable forms to larger, less soluble structures that are likely of lower bioavailability, underscoring the delicate interplay between size, crystallinity, and accessibility. Circumneutral environments with lower concentrations of Fe(II) and HS^- promote formation of smaller, more soluble FeS_{aq} clusters. While higher temperatures promoted FeS_{aq} cluster nucleation and growth, they also promoted FeS_{aq} cluster/particle dissolution. This highlights the dynamic equilibrium that exists between soluble ions, aqueous clusters/particles, and minerals that together influence the availability of Fe and S and thus the distribution of life dependent on these elements. Future research should focus on evaluating similar questions under ferruginous conditions that prevailed when life likely originated, as well as the role of organic ligands on FeS_{aq} cluster nucleation kinetics and stabilization. Such ligands include small peptides such as ferredoxins that commonly bind one or more FeS_{aq} clusters (i.e., 2Fe-2S or 4Fe-4S clusters, as reviewed in [77, 78]) or ferredoxin maquettes featuring the minimal peptide coordination environments for 2Fe-2S or 4Fe-4S clusters those proteins [79–81].

Acknowledgements Computing resources were provided by the Tempest High Performance Computing facility at Montana State University. Funding for the Montana State University Cryo-EM Core Facility (RRID:SCR_026324) was contributed by National Science Foundation (DBI-1828765), the MJ Murdock Charitable Trust, The National Institute of General Medical Sciences (P30GM140963) and the MSU Office of Research, Economic Development and Graduate Education.

Author contribution Manjinder Kour: Investigation, Data Curation, Software, Writing Original Draft. Heather M Callaway: TEM, Writing, Review and Editing. Eric S. Boyd: Supervision, Experimental Design, Writing Original Draft, Review and Editing.

Funding This research was funded by the Division of Chemical Sciences, Geosciences, and Biosciences, Office of Basic Energy Sciences of the U.S. Department of Energy through Grant DE-SC0020246 to ESB.

Data Availability No datasets were generated or analysed during the current study.

Declarations

Competing interests The authors declare no competing interests.

Open Access This article is licensed under a Creative Commons Attribution 4.0 International License, which permits use, sharing, adaptation, distribution and reproduction in any medium or format, as long as you give appropriate credit to the original author(s) and the source, provide a link to the Creative Commons licence, and indicate if changes were made. The images or other third party material in this article are included in the article's Creative Commons licence, unless indicated otherwise in a credit line to the material. If material is not included in the article's Creative Commons licence and your intended use is not permitted by statutory regulation or exceeds the permitted use, you will need to obtain permission directly from the copyright holder. To view a copy of this licence, visit http://creativecommons.org/licenses/by/4.0/.

References

1. Davison W (1977) The polarographic measurement of O_2, Fe^{2+}, Mn^{2+}, and S^{2-} in hypolimnetic water. Limnol Oceanogr 22(4):746–753
2. Davison W, Buffle J, De Vitre R (1988) Interpretation of speciation measurements: a case study. Direct polarographic determination of O_2, Fe(II), Mn(II), S(-II) and related species in anoxic waters. Pure Appl Chem 60(10):1535–1548
3. Theberge SM, Luther GW III (1997) Determination of the electrochemical properties of a soluble aqueous FeS species present in sulfidic solutions. Aquat Geochem 3(3):191–211
4. Rickard D, Oldroyd A, Cramp A (1999) Voltammetric evidence for soluble FeS complexes in anoxic estuarine muds. Estuaries 22:693–701
5. Luther III GW, Glazer BT, Hohmann L, Popp JI, Taillefert M, Rozan TF et al (2001) Sulfur speciation monitored in situ with solid state gold amalgam voltammetric microelectrodes: polysulfides as a special case in sediments, microbial mats and hydrothermal vent waters. J Environ Monitor 3(1):61–66.

6. Taillefert M, Hover V, Rozan TF, Theberge S, Luther G (2002) The influence of sulfides on soluble organic-Fe (III) in anoxic sediment porewaters. Estuaries 25:1088–1096
7. Luther GW, Glazer B, Ma S, Trouwborst R, Shultz BR, Druschel G et al (2003) Iron and sulfur chemistry in a stratified lake: evidence for iron-rich sulfide complexes. Aquat Geochem 9:87–110
8. Burton ED, Johnston SG, Bush RT (2011) Microbial sulfidogenesis in ferrihydrite-rich environments: effects on iron mineralogy and arsenic mobility. Geochim Cosmochim Acta 75(11):3072–3087
9. Burton ED, Bush RT, Johnston SG, Sullivan LA, Keene AF (2011) Sulfur biogeochemical cycling and novel Fe–S mineralization pathways in a tidally re-flooded wetland. Geochim Cosmochim Acta 75(12):3434–3451
10. Hansen DJ, McGuire JT, Mohanty BP, Ziegler BA (2014) Evidence of aqueous iron sulfide clusters in the vadose zone. Vadose Zone J 13:1–12. https://doi.org/10.2136/vzj2013.07.0136
11. Rickard D, Luther GW (2006) Metal sulfide complexes and clusters. Rev Mineral Geochem 61(1):421–504
12. Luther GW, Rickard DT, Theberge S, Olroyd A (1996) Determination of metal (bi) sulfide stability constants of Mn^{2+}, Fe^{2+}, Co^{2+}, Ni^{2+}, Cu^{2+}, and Zn^{2+} by voltammetric methods. Environ Sci Technol 30(2):671–679
13. Canfield DE, Poulton SW, Knoll AH, Narbonne GM, Ross G, Goldberg T et al (2008) Ferruginous conditions dominated later Neoproterozoic deep-water chemistry. Science 321(5891):949–952
14. Poulton SW, Canfield DE (2011) Ferruginous conditions: a dominant feature of the ocean through Earth's history. Elements 7(2):107–112
15. Fakhraee M, Hancisse O, Canfield DE, Crowe SA, Katsev S (2019) Proterozoic seawater sulfate scarcity and the evolution of ocean–atmosphere chemistry. Nat Geosci 12(5):375–380
16. Planavsky NJ, McGoldrick P, Scott CT, Li C, Reinhard CT, Kelly AE et al (2011) Widespread iron-rich conditions in the mid-Proterozoic ocean. Nature 477(7365):448–451
17. Reinhard CT, Raiswell R, Scott C, Anbar AD, Lyons TW (2009) A late Archean sulfidic sea stimulated by early oxidative weathering of the continents. Science 326(5953):713–716
18. Gilleaudeau GJ, Romaniello SJ, Luo G, Kaufman AJ, Zhang F, Klaebe RM et al (2019) Uranium isotope evidence for limited euxinia in mid-Proterozoic oceans. Earth Planet Sci Lett 521:150–157
19. Labrenz M, Druschel GK, Thomsen-Ebert T, Gilbert B, Welch SA, Kemner KM et al (2000) Formation of sphalerite (ZnS) deposits in natural biofilms of sulfate-reducing bacteria. Science 290(5497):1744–1747
20. Wolthers M, Van der Gaast SJ, Rickard D (2003) The structure of disordered mackinawite. Am Mineral 88(11–12):2007–2015
21. Luther GW, Rickard DT (2005) Metal sulfide cluster complexes and their biogeochemical importance in the environment. J Nanopart Res 7:389–407
22. Berner RA (1984) Sedimentary pyrite formation: an update. Geochim Cosmochim Acta 48(4):605–615
23. Schoonen M, Barnes H (1991) Reactions forming pyrite and marcasite from solution: I. Nucleation of FeS_2 below 100 C. Geochim Cosmochim Acta 55(6):1495–1504
24. Rickard D (2006) The solubility of FeS. Geochim Cosmochim Acta 70(23):5779–5789
25. Rickard D, Luther GW (2007) Chemistry of iron sulfides. Chem Rev 107(2):514–562
26. Devey A, Grau-Crespo R, De Leeuw N (2008) Combined density functional theory and interatomic potential study of the bulk and surface structures and properties of the iron sulfide mackinawite (FeS). J Phys Chem C 112(29):10960–10967
27. Kwon KD, Refson K, Sposito G (2015) Transition metal incorporation into mackinawite (tetragonal FeS). Am Mineral 100(7):1509–1517
28. Wolthers M, Charlet L, van Der Linde PR, Rickard D, van Der Weijden CH (2005) Surface chemistry of disordered mackinawite (FeS). Geochim Cosmochim Acta 69(14):3469–3481
29. Matamoros-Veloza A, Stawski TM, Benning LG (2018) Nanoparticle assembly leads to mackinawite formation. Cryst Growth Des 18(11):6757–6764
30. Scherer P, Sahm H (1981) Influence of sulphur-containing compounds on the growth of *Methanosarcina barkeri* in a defined medium. Eur J Appl Microbiol Biotechnol 12:28–35
31. Payne D, Shepard EM, Spietz RL, Steward K, Brumfield S, Young M et al (2021) Examining pathways of iron and sulfur acquisition, trafficking, deployment, and storage in mineral-grown methanogen cells. J Bacteriol 203(19). https://doi.org/10.1128/jb.00146-21
32. Payne D, Spietz RL, Boyd ES (2021) Reductive dissolution of pyrite by methanogenic archaea. ISME J 15(12):3498–3507
33. Payne D, Spietz RL, Newell DL, Dijkstra P, Boyd ES (2023) Influence of sulfide on diazotrophic growth of the methanogen *Methanococcus maripaludis* and its implications for the origin of nitrogenase. Commun Biol 6(1):799
34. Spietz RL, Payne D, Kulkarni G, Metcalf WW, Roden EE, Boyd ES (2022) Investigating abiotic and biotic mechanisms of pyrite reduction. Front Microbiol 13:878387
35. Spietz RL, Payne D, Boyd ES (2022) Reductive biomining of pyrite by methanogens. Trends Microbiol 30(11):1072–1083
36. Boyd ES, Payne D (2025) Expanded diversity of microbial groups capable of anaerobic pyrite reduction and assimilation of dissolution products. Environ Microbiol 27: e70125
37. Johnson DC, Dean DR, Smith AD, Johnson MK (2005) Structure, function, and formation of biological iron-sulfur clusters. Annu Rev Biochem 74(1):247–281
38. Beinert H, Holm RH, Munck E (1997) Iron-sulfur clusters: nature's modular, multipurpose structures. Science 277(5326):653–659
39. Chai J-D, Head-Gordon M (2008) Long-range corrected hybrid density functionals with damped atom–atom dispersion corrections. Phys Chem Chem Phys 10(44):6615–6620
40. Weigend F, Ahlrichs R (2005) Balanced basis sets of split valence, triple zeta valence and quadruple zeta

valence quality for H to Rn: design and assessment of accuracy. Phys Chem Chem Phys 7(18):3297–3305
41. Bergerhoff G, Hundt R, Sievers R, Brown I (1983) The inorganic crystal structure data base. J Chem Inf Comput Sci 23(2):66–69
42. Frisch MJ, Trucks GW, Schlegel HB, Scuseria GE, Robb MA, Cheeseman JR et al (2016) Gaussian 16 Rev. C.01. Wallingford
43. Shoji M, Koizumi K, Kitagawa Y, Kawakami T, Yamanaka S, Okumura M et al (2006) A general algorithm for calculation of Heisenberg exchange integrals J in multispin systems. Chem Phys Lett 432(1–3):343–347
44. Davidson ER, Clark AE (2007) Analysis of wave functions for open-shell molecules. Phys Chem Chem Phys 9(16):1881–1894
45. Kour M, Taborosi A, Boyd ES, Szilagyi RK (2023) Development of molecular cluster models to probe pyrite surface reactivity. J Comput Chem 44(32):2486–2500
46. Marenich AV, Cramer CJ, Truhlar DG (2009) Universal solvation model based on solute electron density and on a continuum model of the solvent defined by the bulk dielectric constant and atomic surface tensions. J Phys Chem B 113(18):6378–6396
47. Hassan PA, Rana S, Verma G (2015) Making sense of Brownian motion: colloid characterization by dynamic light scattering. Langmuir 31(1):3–12
48. Pecora R (2000) Dynamic light scattering measurement of nanometer particles in liquids. J Nanopart Res 2:123–131
49. Blanco-Andujar C, Ortega D, Pankhurst QA, Thanh NTK (2012) Elucidating the morphological and structural evolution of iron oxide nanoparticles formed by sodium carbonate in aqueous medium. J Mater Chem 22(25):12498–12506
50. Csákberényi-Malasics D, Rodriguez-Blanco JD, Kis VK, Rečnik A, Benning LG, Pósfai M (2012) Structural properties and transformations of precipitated FeS. Chem Geol 294:249–258
51. Kahl W-A, Klügel A, Bach W, Mangir MM (2022) Enhanced weathering in the seabed: rapid olivine dissolution and iron sulfide formation in submarine volcanic ash. Am Miner 107(9):1668–1680
52. Zhu F, Peng X, Hu X, Kong L (2022) H_2S release rate strongly affects particle size and settling performance of metal sulfides in acidic wastewater: the role of homogeneous and heterogeneous nucleation. J Hazard Mater 438:129484
53. Stetefeld J, McKenna SA, Patel TR (2016) Dynamic light scattering: a practical guide and applications in biomedical sciences. Biophys Rev 8:409–427
54. Ahuja R, Sidhu A, Bala A (2019) Synthesis and evaluation of iron (II) sulfide aqua nanoparticles (FeS-NPs) against *Fusarium verticillioides* causing sheath rot and seed discoloration of rice. Eur J Plant Pathol 155:163–171
55. Agnihotri S, Mohan T, Jha D, Gautam HK, Roy I (2020) Dual modality FeS nanoparticles with reactive oxygen species-induced and photothermal toxicity toward pathogenic bacteria. ACS Omega 5(1):597–602
56. Yuan Y, Wang L, Gao L (2020) Nano-sized iron sulfide: structure, synthesis, properties, and biomedical applications. Front Chem 8:818
57. Kelton K, Greer A (2010) The classical theory. Pergamon Materials Series. Elsevier, p 19–54
58. Noël V, Kumar N, Boye K, Barragan L, Lezama-Pacheco JS, Chu R et al (2020) FeS colloids–formation and mobilization pathways in natural waters. Environ Sci Nano 7(7):2102–2116
59. Spielman-Sun E, Boye K, Dwivedi D, Engel M, Thompson A, Kumar N et al (2024) A critical look at colloid generation, stability, and transport in redox-dynamic environments: challenges and perspectives. ACS Earth Space Chem 8(4):630–653
60. Yang H, Hong M, Chen S (2020) Removal of Cr (VI) with nano-FeS and CMC-FeS and transport properties in porous media. Environ Technol 41(22):2935–2945
61. Liao P, Yuan S, Wang D (2016) Impact of redox reactions on colloid transport in saturated porous media: an example of ferrihydrite colloids transport in the presence of sulfide. Environ Sci Technol 50(20):10968–10977
62. Mitra-Delmotte G, Mitra A (2010) Magnetism, FeS colloids, and origins of life. The legacy of alladi ramakrishnan in the mathematical sciences. Springer, pp 529–564
63. He L, Xie L, Wang D, Li W, Fortner JD, Li Q et al (2019) Elucidating the role of sulfide on the stability of ferrihydrite colloids under anoxic conditions. Environ Sci Technol 53(8):4173–4184
64. O'Hayre R (2015) Materials kinetics fundamentals. John Wiley & Sons
65. Wang QL, Zhang Z, Kan A, Tomson M (2014) Kinetics and inhibition of ferrous sulfide nucleation and precipitation. SPE International Oilfield Scale Conference and Exhibition: SPE, p D022S12R02
66. Thiel J, Byrne JM, Kappler A, Schink B, Pester M (2019) Pyrite formation from FeS and H_2S is mediated through microbial redox activity. Proc Natl Acad Sci 116(14):6897–6902
67. Lang SM, Miyajima K, Bernhardt TM, Mafuné F, Barnett RN, Landman U (2018) Thermal stability of iron–sulfur clusters. Phys Chem Chem Phys 20(11):7781–7790
68. Luther GW III, Glazer BT, Ma S, Trouwborst RE, Moore TS, Metzger E et al (2008) Use of voltammetric solid-state (micro) electrodes for studying biogeochemical processes: laboratory measurements to real time measurements with an in situ electrochemical analyzer (ISEA). Mar Chem 108(3–4):221–235
69. Prieur D, Erauso G, Jeanthon C (1995) Hyperthermophilic life at deep-sea hydrothermal vents. Planet Space Sci 43(1–2):115–122
70. Major TA, Burd H, Whitman WB (2004) Abundance of 4Fe–4S motifs in the genomes of methanogens and other prokaryotes. FEMS Microbiol Lett 239(1):117–123
71. Amend JP, Shock EL (2001) Energetics of overall metabolic reactions of thermophilic and hyperthermophilic archaea and bacteria. FEMS Microbiol Rev 25(2):175–243

72. Luther GW III, Findlay AJ, MacDonald DJ, Owings SM, Hanson TE, Beinart RA et al (2011) Thermodynamics and kinetics of sulfide oxidation by oxygen: a look at inorganically controlled reactions and biologically mediated processes in the environment. Front Microbiol 2:62
73. Drzaic PS, Marks J, Brauman JI (1984) Electron photodetachment from gas phase molecular anions. Ions and Light. Elsevier, pp 167–211
74. Radzig AA, Smirnov BM (2012) Reference data on atoms, molecules, and ions. Springer Series in Chemical Physics Springer-Berlin, Heidelberg
75. Matamoros-Veloza A, Cespedes O, Johnson BR, Stawski TM, Terranova U, de Leeuw NH et al (2018) A highly reactive precursor in the iron sulfide system. Nat Commun 9(1):3125
76. Niederberger M, Cölfen H (2006) Oriented attachment and mesocrystals: non-classical crystallization mechanisms based on nanoparticle assembly. Phys Chem Chem Phys 8(28):3271–3287
77. Bruschi M, Guerlesquin F (1988) Structure, function and evolution of bacterial ferredoxins. FEMS Microbiol Lett 54(2):155–175
78. Buckel W, Thauer RK (2018) Flavin-based electron bifurcation, ferredoxin, flavodoxin, and anaerobic respiration with protons (Ech) or NAD^+ (Rnf) as electron acceptors: a historical review. Front Microbiol 9:401
79. Galambas A, Miller J, Jones M, McDaniel E, Lukes M, Watts H et al (2019) Radical S-adenosylmethionine maquette chemistry: Cx3Cx2C peptide coordinated redox active [4Fe–4S] clusters. J Biol Inorg Chem 24:793–807
80. Gibney BR, Mulholland SE, Rabanal F, Dutton PL (1996) Ferredoxin and ferredoxin–heme maquettes. Proc Natl Acad Sci USA 93(26):15041–15046
81. Mulholland SE, Gibney BR, Rabanal F, Dutton PL (1999) Determination of nonligand amino acids critical to $[4Fe\text{-}4S]^{2+/+}$ assembly in ferredoxin maquettes. Biochemistry 38(32):10442–10448

Publisher's Note Springer Nature remains neutral with regard to jurisdictional claims in published maps and institutional affiliations.